Optics and Lasers in Engineering 163 (2023) 107444

Contents lists available at ScienceDirect

Optics and Lasers in Engineering

journal homepage: www.elsevier.com/locate/optlaseng

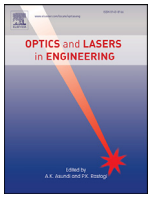

Identification of defects in composite laminates by comparison of mode shapes from electronic speckle pattern interferometry

X.N. Li [a,b,*], P.C. Sung [b], E.A. Patterson [a], W.C. Wang [b], W.J.R. Christian [a]

[a] School of Engineering, University of Liverpool, L69 3GH, UK
[b] Department of Power Mechanical Engineering, National Tsing Hua University, Hsinchu, Taiwan

ARTICLE INFO

Keywords:
Carbon fibre reinforced polymer
Fibre waviness
AF-ESPI
Modal analysis
Fourier descriptors

ABSTRACT

A novel technique for identifying defects in carbon fibre reinforced plates has been developed. Firstly, modal analysis by impact excitation was performed to obtain the first five resonant frequencies for three defect-free and three defective specimens with in-plane fibre waviness. Then amplitude-fluctuation electronic speckle pattern interferometry (AF-ESPI) was used to obtain the mode shapes at these frequencies. The contours of the nodal regions visible in the mode shapes were extracted using a specially-developed algorithm employing density-based spatial clustering of applications with noise (DBSCAN). Fourier descriptors, that are invariant to rotations, translations, and scaling, were used to decompose the contours to reduce data dimensionality and make comparisons. The differences in contours between the two sets of specimens showed that the 4th and 5th mode shapes can be used for identifying the presence of the waviness defects. This technique for nodal region comparison was found to greatly simplify the comparison of fringe patterns for the purpose of damage assessment and could potentially be used as part of validation procedures.

1. Introduction

Carbon fibre reinforced polymer (CFRP) is a promising material that can provide superior stiffness and strength combined with low weight and is thus widely used in the aerospace industry. However, the misorientation of fibres in composite components, referred to as fibre waviness, can reduce the service life of composite components. Numerous investigations have focused on the reduction of mechanical properties caused by fibre waviness, as reviewed in [1], but little experimental research has explored its effect on the vibration behaviour of composites.

Studies have shown that natural frequencies and vibration modes of unidirectional CFRP laminates change with different fibre orientations, e.g. 0°, 45° and 90°, and that the change in the stiffness of the laminates was the main cause [2]. Similar findings in [3] showed a reduction in resonant frequencies of the first two modes for laminates made of glass fibre reinforced polymers, due to an increase in fibre orientation from 0° to 90°, when six fibre orientations were investigated: 0°, 30°, 45°, 60° and 90°. These findings consider the effects of specific fibre orientations, but fibres with random alignments, such as when fibre waviness is present, have not been experimentally studied. The most recent work conducted to investigate the effect of fibre waviness on vibration behaviour was in [4], where using analytical and numerical methods, it was found that fibre waviness caused a reduction in resonant frequencies for certain modes. This effect was predicted to be more significant if the waviness defect occurred in the plies that contributed more stiffness to the laminate. They also found that bending modes are more susceptible to waviness defects that occurred in the 0° ply. However, whether the mode shapes of CFRP components would be affected by fibre waviness has not been explored by any subsequent research.

Electronic speckle pattern interferometry (ESPI) is a non-destructive and full-field measurement technique that can be used to measure small displacements with a high spatial resolution [5]. The high spatial resolution enables the technique to measure the vibration mode shapes of materials in real time. Time-averaged ESPI has been used to obtain mode shapes of a vibrating plate, which were compared with results from analytical methods and showed good agreement, but the authors noticed a decrease in contrast for some fringes [6]. Both the visibility and spatial resolution of the fringe pattern can be significantly improved when using amplitude-fluctuation electronic speckle pattern interferometry (AF-ESPI). The quality of fringe patterns can be further improved by also using radial basis functions as a pre-filtering method to remove noise [7]. AF-ESPI has been used to identify pre-cut square and circular defects in composite plates based on changes in mode shapes, with the effects of the defects being more visible in the fringe patterns for higher modes [8]. Interfacial cracks can also be detected using AF-ESPI by comparing the fringe patterns of specimens with and without defects [9]. Whilst these studies could identify defects by comparing fringe patterns for defective and non-defective specimens, these comparisons were made

* Corresponding author at: School of Engineering, University of Liverpool, L69 3GH, UK.
E-mail address: Xiaonan.Li@liverpool.ac.uk (X.N. Li).

https://doi.org/10.1016/j.optlaseng.2022.107444
Received 2 June 2022; Received in revised form 18 December 2022; Accepted 18 December 2022

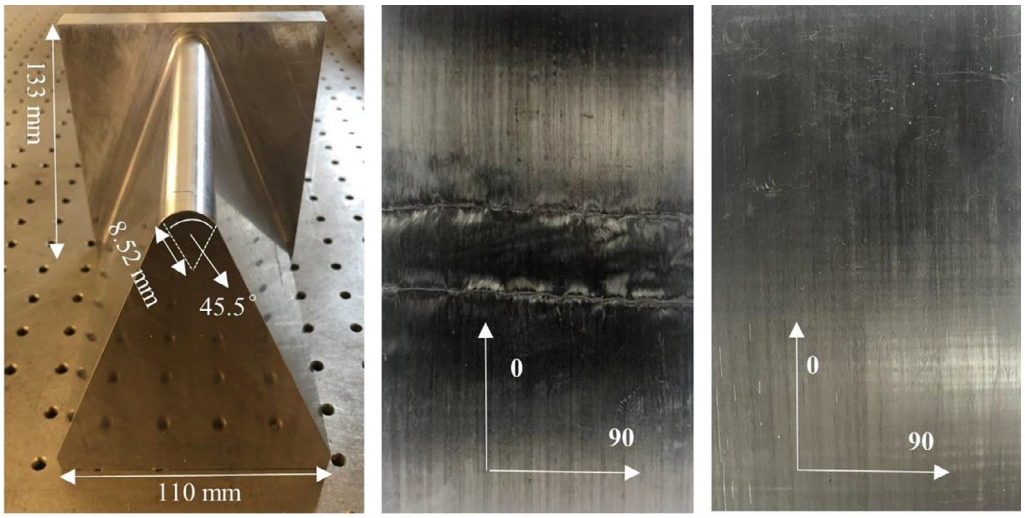

Fig. 1. An aluminium former for creating localised fibre waviness (left), the top surface of a defective specimen with in-plane waviness in the top ply (middle), and the bottom side (right). The 0° fibres were aligned along the length of the laminate.

qualitatively. In order to make quantified comparisons, this study introduces a novel image processing technique that combines the density-based spatial clustering of applications with noise (DBSCAN) algorithm and contour decomposition using Fourier descriptors. This was used to quantify the difference between the nodal regions of mode shapes and thus identify the presence of fibre-waviness defects.

2. Experimental methods

2.1. Specimen preparation

Carbon fibre reinforced cross-ply laminates, with a stacking sequence of $[0_2/90_2/0_2/90_2]_s$, were manufactured using unidirectional prepreg (RP542-4UT300, PRF, UK). Three defect-free specimens were first manufactured to serve as a benchmark set. Three defective composite specimens were then manufactured using the method described in [10] to induce a band of in-plane fibre waviness across the width of the laminates. For simplicity, the term "waviness" in the following text refers to in-plane fibre waviness. The waviness defects were formed using a special aluminium former, as shown in Fig. 1 left. Each ply was laid on top of the former in the predetermined stacking sequence to create a laminate. The V-shaped laminate was then removed from the former and flattened by hand. The fibres in the top ply, at the tip of the V-shape, buckled to compensate for the length difference between the top ply and the bottom ply after the laminate had been flattened. This created a localised band of in-plane waviness at the middle of each specimen on the top ply, as shown in Fig. 1 middle.

The laminates were cured in a hot press (APV-2525, Meyer, Germany), by heating them up to 120 °C from room temperature (23 °C), at a heating rate of 1 °C/min. After heating, they were held at 120 °C for 1 h. The hot press pressure was set to 2.5 bar during heating, curing and cooling. Once the laminates were cured, the hot press was left to naturally cool to room temperature. After removal from the hot press, each specimen was cut using a wet diamond saw (Versatile 103450, Vitrex, USA) to a size of 150 mm by 100 mm. The average thickness of the specimens was 3.72 mm. A typical defective specimen is shown in Fig. 1, with one side having in-plane fibre waviness in the top ply and the bottom ply containing no waviness. The top surface of each specimen was then sprayed with a layer of white powder (D-70, Mel-L-Chek, USA) to prevent specular reflections during the AF-ESPI testing.

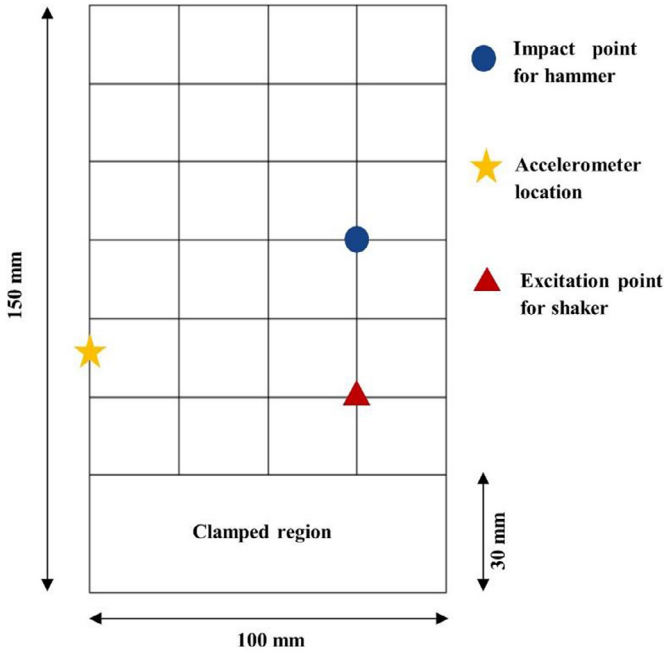

Fig. 2. Diagram showing the excitation positions for the impact and shaker, accelerometer location and clamped region of each specimen.

2.2. Modal analysis by impact excitation

Modal analysis by impact excitation was performed on each specimen to find its resonant frequencies. Each specimen was impacted by a hammer (PCB, 086B01, USA) at one point and the response was measured at another point by an accelerometer (PCB, 352C22, USA). The impact and measurement points were determined after a few pre-tests to make sure that clear peaks in the frequency response function (FRF) curve were observed. The selected points are shown in Fig. 2. Each specimen being tested was clamped by a vice and attached to a stinger. The vice was attached to an optical table and the stinger was connected to a shaker (Labworks, ET-132, USA). The impact-based modal analysis was performed on the specimens whilst the shaker was turned off. For the defective specimens, the non-wavy side was selected to attach the

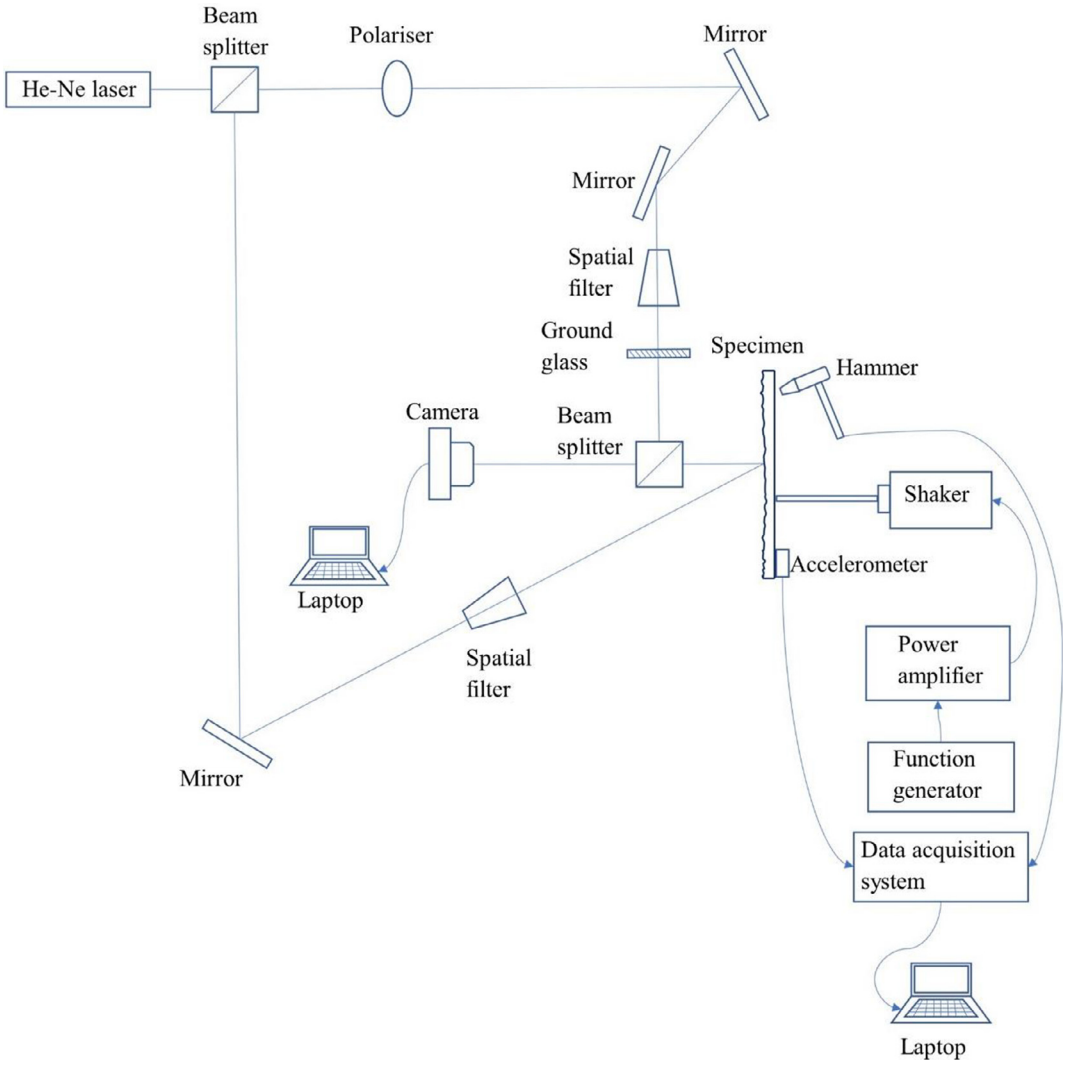

Fig. 3. Schematic of the AF-ESPI and modal analysis set-ups.

accelerometer and the stinger, this side was also the side impacted by the hammer. The accelerometer output was recorded by a data acquisition system (National Instruments, NI 9234, USA) with a USB adaptor (National Instruments, NI USB-9162, USA). The acquired data was then processed by a commercial software (M+P International, Germany) on a laptop to calculate the frequency response functions and obtain the first five resonant frequencies for each specimen. The schematic drawing of the modal analysis by impact excitation is shown in Fig. 3.

2.3. Modal analysis by shaker excitation combined with AF-ESPI technique

The specimens were excited by a shaker connected by a stinger to the excitation point. Sine waves provided by a function generator (Agilent, 33220A, USA) were set sequentially to the five resonant frequencies obtained by the impact-based modal analysis for each specimen, and the analogue signals were amplified by a power amplifier (Labworks, PA-138, USA) before being transmitted to the shaker. AF-ESPI was performed on each specimen to obtain the mode shapes while the shaker loaded the specimens at each resonant frequency. The AF-ESPI set-up is shown in Fig. 3. Coherent light was provided by a He-Ne laser (Spectra-Physics, 12735, USA), and split into two beams, where one was a reference beam and the other was an object beam. The object beam arrived at the specimen and then was reflected. The reflected object beam together with the reference beam went back to a camera (Intelliwave, RS170, USA) generating interference speckle patterns, which contained information on the interferometric measurement of surface displacements during vibrations at the resonant frequencies.

Unlike traditional ESPI using video-signal-addition or video-signal-subtraction methods, the reference image was not taken when the shaker was turned off and the specimen was stationary. Instead, for the AF-ESPI technique, a reference image was taken at each resonant frequency of the specimen at one instant during the vibrations, and another image was taken afterwards at the same frequency and subtracted from the reference image. The difference between these two image signals was converted into a greyscale image using the image processing system (Intelliwave, v6.7.1, USA), resulting in an interference fringe pattern.

3. Results

An example of the FRF for one of the specimens is shown in Fig. 4. The FRF was obtained by analysing the acquired data from modal analysis by impact excitation. The FRF was divided into a real part and an imaginary part. The first five resonant frequencies were identified as the peaks of the curve in the imaginary part, which also corresponded to abrupt changes to the curve in the real part. The first five resonant frequencies for all the specimens are shown in Table 1.

Fringe patterns were obtained from the modal analysis combined with the AF-ESPI technique when each specimen was excited using

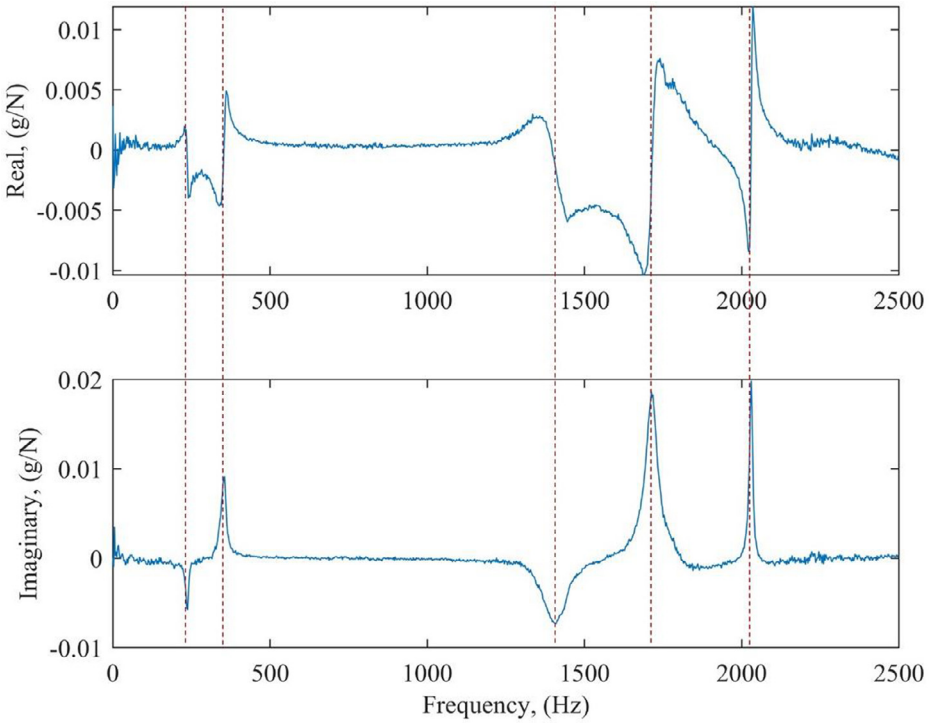

Fig. 4. Frequency response function of a defect-free specimen with top plot showing the real part and bottom showing the imaginary part. The first 5 resonant frequencies are indicated by dashed lines.

Table 1
Resonant frequencies of the first five modes obtained from the modal analysis by impact excitation for the three defect-free and three defective specimens.

Specimen Type and No.	1st mode (Hz)	2nd mode (Hz)	3rd mode (Hz)	4th mode (Hz)	5th mode (Hz)
No defect #1	240	350	1405	1718	2028
No defect #2	238	355	1425	1725	2024
No defect #3	238	355	1410	1712	2030
Defective #1	238	348	1490	1715	2115
Defective #2	255	375	1558	1725	2123
Defective #3	255	378	1550	1733	2113
Mean of no defect	239	353	1413	1718	2027
Mean of defective	249	367	1533	1724	2088
Difference between the two means in percent	4.2%	4.0%	8.5%	0.3%	3.0%

the shaker, as shown in Fig. 5, representing the five vibration modes for all the specimens. The fringe patterns for the defect-free specimens are shown in the left three columns, while the fringe patterns for the defective specimens are shown in the right three columns. Each one of the five rows of the patterns shows the mode shapes from the 1st mode to the 5th mode respectively. It can be observed that both the 1st and the 3rd mode are pure bending modes, both the 2nd and the 5th mode are pure twisting modes, and the 4th mode is a mixed mode of bending and twisting. For the sake of reproducibility of the tests and repeatability of the results, the experimental set-ups have been dismantled and reassembled six times. Modal analysis combined with the AF-ESPI technique were also performed six times on one defective specimen and one defect-free specimen to ensure that the resonant frequencies and fringe patterns obtained for the first five modes were consistent.

The extraction process for the contour of the nodal region was performed by a specially developed algorithm, as shown in Fig. 6. The original fringe pattern is a greyscale image. The largest bright fringe is not clearly separated from the other fringes, therefore the mean image intensity was subtracted from every individual pixel, which is a common procedure in the field of computer vision and deep learning to reveal features of interest [11]. The mean-subtracted image was then binarized by adaptive thresholding. The threshold was set by calculating the mean pixel intensity within a window of size, s, around each pixel. The value of each pixel was set to black if its value was lower than the threshold for its window, otherwise it was set to white. The window size, s was set to 1/8 of the image width, as suggested in [12]. The binarized image was then divided into several clusters using the density-based spatial clustering of applications with noise algorithm (DBSCAN), where each colour is represented a cluster, as shown in Fig. 6. Two important parameters for using the DBSCAN algorithm are the searching radius and the minimum number of points to be considered as a cluster. The principle of the DBSCAN is to identify three different types of points: the core points, which are the minimum number of points within the searching radius to form a cluster, thus each cluster has the same density; the border points, which are located at the searching radius of the core points, but do not have the minimum number of points in their own searching radius to form a cluster; and noise points, which are outliers [13]. The core points are the interior points of clusters, and the border points are the boundaries of the clusters. Clusters cannot be combined into a single cluster if they do not share a core point. The minimum number of points to form a cluster was set to the default value of 4, as the data was

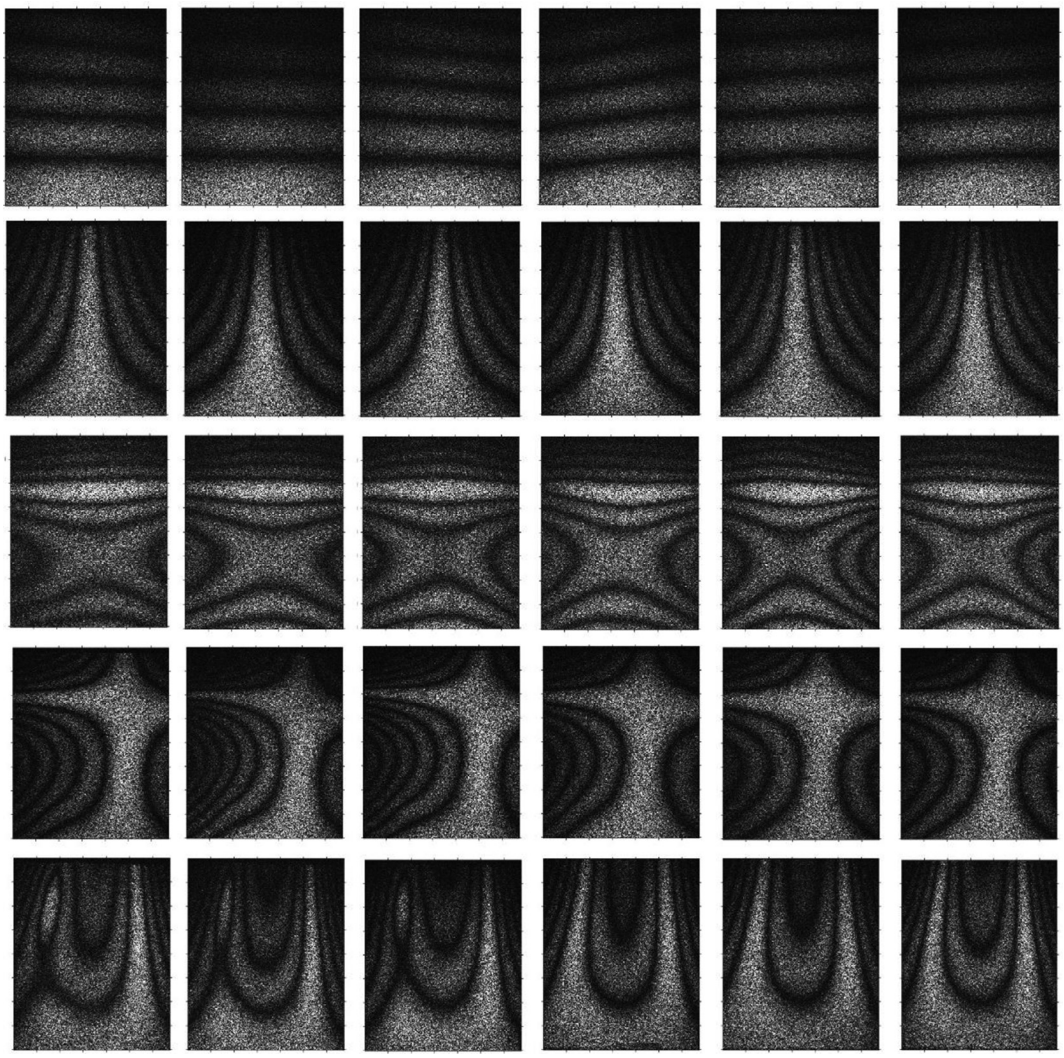

Fig. 5. Electronic fringe patterns obtained using AF-ESPI at the resonant frequencies for the six specimens. Each row shows the fringe patterns corresponding to the 1st (top) to the 5th (bottom) mode shape. The left three columns of the fringe patterns show the mode shapes for the defect-free specimens, the right three columns show the mode shapes for the defective specimens.

two-dimensional [14]. For each point in the binarized image, the 4th nearest point to it was found and the Euclidean distance between them was calculated as the 4th nearest distance for this point. The searching radius was determined by calculating the 4th nearest distances for all the points and sorting the points by ascending order of the 4th nearest distances, resulting in the curve shown in Fig. 7. The point at which the curve starts to significantly increase, referred to as the knee point of the curve, was identified by finding the location on the curve which formed the largest perpendicular distance to a straight line connecting the start and end point of the curve, as shown in Fig. 7. The searching radius was set to the 4th nearest distance corresponding to this knee point. The nodal region can then be easily identified as the cluster with the largest area. The algorithm can automatically select the nodal regions from most of the fringe patterns, except for those of the defect-free specimens for the 5th mode. This is because there is a small bright fringe close to the largest bright fringe with approximately the same level of brightness, which was identified as a detached part of the main nodal region. Therefore, the cluster formed from this small fringe for the 5th mode of the defect-free specimens was manually selected. The contour representing the nodal region was extracted as the borderline of the cluster.

The comparison of the fringe patterns representing mode shapes was performed by comparing the extracted contours of the nodal regions. The contours for the 1st and the 3rd mode shape of all the specimens appear to be largely horizontal lines that lack significant features which can be used for comparison. Therefore, only the 2nd, 4th and 5th modes were selected for comparisons, where the 2nd mode was mainly used as a benchmark mode. Each contour for the three selected mode shapes was decomposed into a number of Fourier descriptors. First, the Fourier spectrum was obtained by applying the discrete Fourier transform to the complex form of the Cartesian coordinates defining the contour. The terms in the Fourier spectrum were listed as follows:

$$FS = \left[F_0,\ F_1, F_2, \ldots,\ F_{L-1}\right] \tag{1}$$

The length of the Fourier spectrum, L, was equal to the number of points in the coordinate system. The sequence of the terms in the Fourier spectrum was then rearranged as:

$$FS_{rearranged} = \left[F_{\frac{L}{2}},\ \ldots, F_{L-2},\ F_{L-1},\ F_0,\ F_1, F_2, \ldots,\ F_{\frac{L}{2}-1}\right] \tag{2}$$

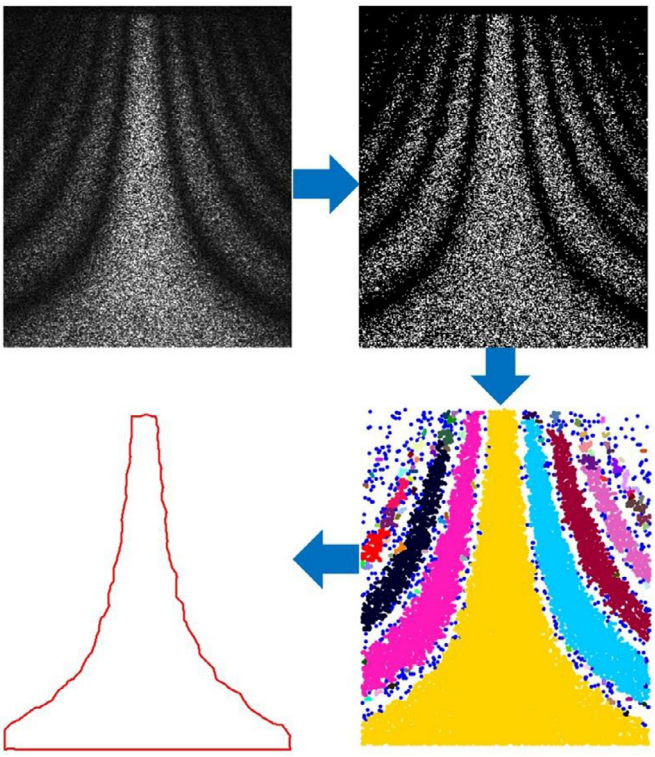

Fig. 6. The extraction process of the nodal region from a fringe pattern of the 2nd mode showing: the original fringe pattern in greyscale (top left); binarised fringe pattern (top right); clustered areas after applying the DBSCAN algorithm (bottom right); contour extraction (bottom left).

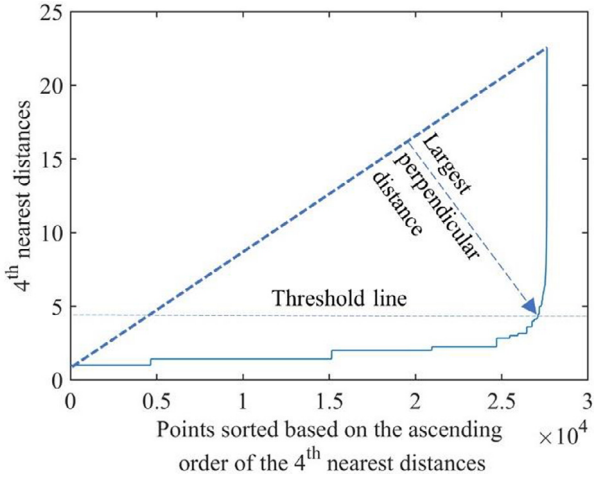

Fig. 7. The determination of the threshold value for the searching radius when forming a cluster. All the points of a contour were sorted based on the 4th nearest pairwise Euclidean distance of each point in ascending order and plotted. The threshold was identified by finding the largest perpendicular distance from the line linking the start and end point of the curve to any point on the curve.

The Fourier descriptors were calculated from $FS_{rearranged}$ using the equation given in [15], with the notation modified for clarity as:

$$FD = \frac{1}{|F_1|} \cdot \left[\left| F_{\frac{N}{2}} \right|, \ldots, |F_{N-2}|, |F_{N-1}|, |F_2|, |F_3|, \ldots, \left| F_{\frac{N}{2}-1} \right| \right] \quad (3)$$

where F_i is the i^{th} term in the Fourier spectrum, N is an even number, representing the number of Fourier descriptors, and $N \leq L$. It was not possible to reconstruct the contours directly from the Fourier descriptors as they were real valued, which was not an appropriate input for the inverse discrete Fourier transform. Therefore, when reconstructing a contour, the same range in the Fourier spectrum as the Fourier descriptors was used, i.e., the terms from $F_{\frac{N}{2}}$ to $F_{\frac{N}{2}-1}$ in the $FS_{rearranged}$. These terms were converted into the complex form of the Cartesian coordinates using the inverse discrete Fourier transform, and the reconstruction was obtained by plotting the real components against the imaginary components.

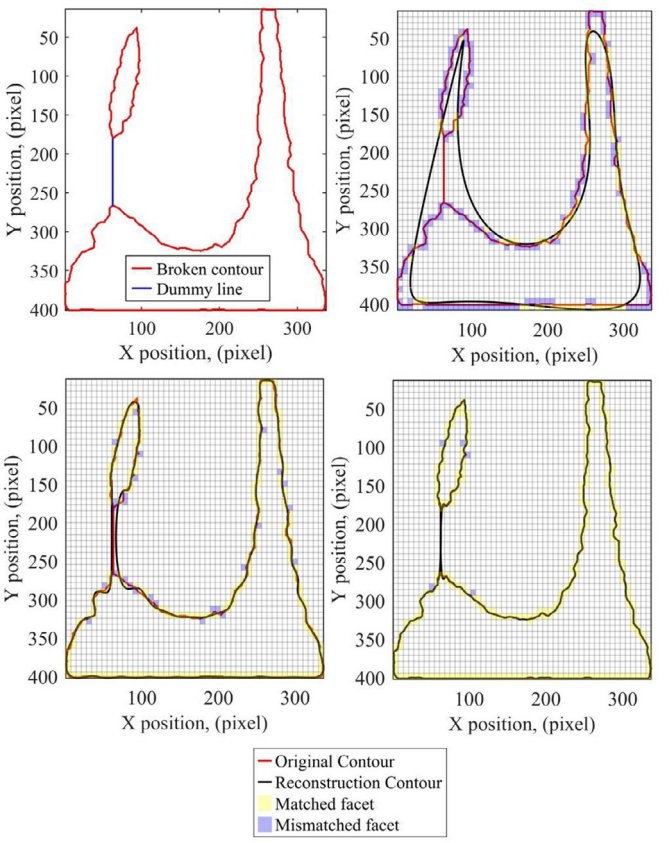

Fig. 8. The approach for combining the broken contours of the 5th mode shape of a defect free specimen before decomposing using Fourier descriptors (top left). The original and reconstructed contours using 10 terms (top right), 90 terms (bottom left) and 380 terms (bottom right). The contour map was meshed into 2500 facets, with the matched facets labelled yellow and mismatched facets labelled blue.

The contours are all closed curves except for the three 5th mode nodal regions of the defect-free specimens, which each have two separate contours. Fourier descriptors can only be used to decompose a closed contour [16], so two dummy lines were used to link the two separate contours. The two dummy lines were created by finding the two nearest points, A and B, on the two separate contours, and then the separate contours were made into a closed one by creating a loop using the two dummy lines A-B and B-A. It should be noted that there are no points between A and B on the dummy lines. An example of the fixed contour for the 5th mode is shown in Fig. 8. The quality of the reconstruction from the feature vector varied with the number of terms in the vector. To evaluate the quality of the reconstruction, each image was meshed into 2500 facets, using a facet size equal to 2% of the length of the binary image. The facets which had both the original and reconstructed contours passing through them were considered matched facets, and the facets through which only the original contour passed through were considered mismatched facets. The percentage of the mismatched facets P was then calculated as follows:

$$P = \frac{Number\ of\ mismatched\ facets}{Number\ of\ matched\ facets + Number\ of\ mismatched\ facets} \quad (4)$$

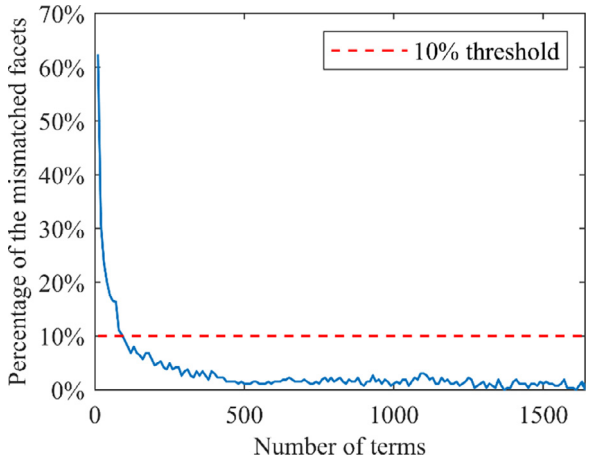

Fig. 9. The diagram showing the relationship between the number of Fourier descriptors and the reconstruction quality of the contour shown in Fig. 8. The reconstruction quality is represented by the percentage of mismatched facets. The threshold is set to 10% to identify when an acceptable representation is attained.

A criterion of $P \leq 10\%$ was used to identify that the reconstruction was acceptable. For the contour shown in Fig. 8, the criterion was satisfied when 90 terms were used, as shown in Fig. 9. The reconstructions using 10, 90 and 380 terms, respectively are shown in Fig. 8. Ninety terms were found to be sufficient to achieve an acceptable reconstruction for all of the contours, therefore 90 Fourier descriptors were used for decomposing all of them.

The Fourier descriptors as calculated using expression (3) are scale invariant, rotation invariant and translation invariant when being used to represent images [17]. This invariance characteristic was verified by processing two contours representing the 2nd and 4th mode shape of one defect-free specimen in three ways: firstly, by rotating the contour by 30° anticlockwise; secondly, by translating the contour down and to the right by 50 pixels; and thirdly, by rescaling the contour to be 50% of its original size. The original and three new contours of the 4th mode are shown in Fig. 10. Each contour was then decomposed into 90 Fourier descriptors to yield feature vectors. The Euclidean distance between pairs of these feature vectors was calculated and is shown as a correlation matrix in Fig. 11. Another popular distance metric, known as the Pearson correlation coefficient, was not selected in this study to measure the similarities between the feature vectors, due to the fact that it measures the linear correlation between any two sets of data. This means the Pearson correlation coefficient cannot provide enough contrast to distinguish between feature vectors when used to generate a correlation matrix.

As shown in Fig. 12, three correlation matrices were obtained by comparing the contours of the 2nd, 4th, and 5th vibration mode for the three defective specimens and three defect-free specimens. Each value in the correlation matrices is the Euclidean distance between pairwise feature vectors. The Euclidean distance between any pair of feature vectors representing defect-free specimens was considered as background noise, ed_{noise}; whereas the Euclidean distance between any pair of feature vectors representing defective and defect-free specimens was considered as desired signals, ed_{signal}. Therefore, a ratio r_i, analogous to a signal to noise ratio, was defined as follows:

$$r_i = \frac{E_i\left[ed_{signal}\right]}{E_i\left[ed_{noise}\right]} \tag{5}$$

where i is the mode number, and the value of i is 2, 4, and 5, respectively; E_i refers to the expected value. The ratios calculated from the correlation matrices in Fig. 12 are that r_2 is 1.88, r_4 is 4.67, and r_5 is 6.14.

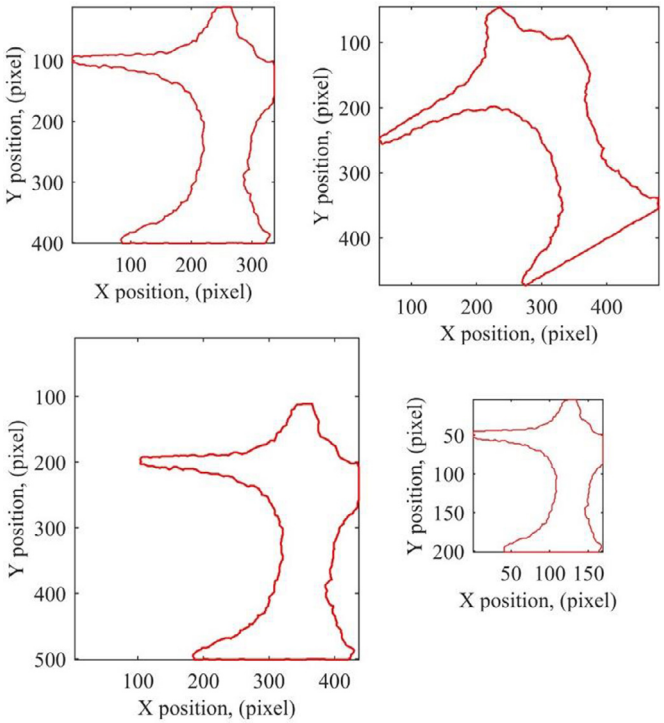

Fig. 10. The original contour of the 4th mode for a defect free specimen (top left). The contour transformed by being: rotated 30° anticlockwise (top right), translated towards the bottom right corner vertically and horizontally by 50 pixels (bottom left), and scaled by shrinking by 50% (bottom right).

4. Discussion

The effect of in-plane waviness on the resonant frequencies was found to vary with different modes. As shown in Table 1, the differences between the mean resonant frequency of the defect-free and defective specimens at their 1st, 2nd, 4th, and 5th mode are less than 5%, and that the difference for the 3rd mode is approximately 8%. The potential reason for this variation is because the fibre waviness was created with the most misorientated fibres aligned along the 90° fibre direction in the top ply, as shown in Fig. 1. This caused a major change in the stiffness of the defective ply. The difference in the mean resonant frequencies of the 3rd mode is the highest, which is consistent with the bending modes being more sensitive to fibre waviness [4], and that the AF-ESPI is more sensitive to defects for higher modes [8].

The nodal regions in each of the specimens are similar for the 1st, 2nd and 3rd modes, whilst more differences are observed for the 4th and 5th modes. This is based on visually inspecting the fringe patterns in Fig. 5. The reason for selecting the nodal regions for comparison is that they are a key characteristic of a vibrating system, which is affected by changes in the stiffness of specimens due to the existence of defects such as fibre waviness. The procedure for extracting the nodal region is shown in Fig. 6, where not only the general shape of the nodal region is extracted from the fringe patterns, but also the details of its contour are acquired. It should be noted that some of the roughness on the contours resulted from the measurement technique, which caused additional random electronic speckles in the fringe patterns. So, the extracted contour is a close approximation of the true nodal region. The aim of comparing the contours of mode shapes was to investigate if fibre waviness existed, so the focus was on comparing the general shape of the nodal regions, not small variations along the contour.

Rather than using intuition to select the number of Fourier descriptors to use during decomposition, a new method was introduced in this study to identify whether the contour is accurately represented. This

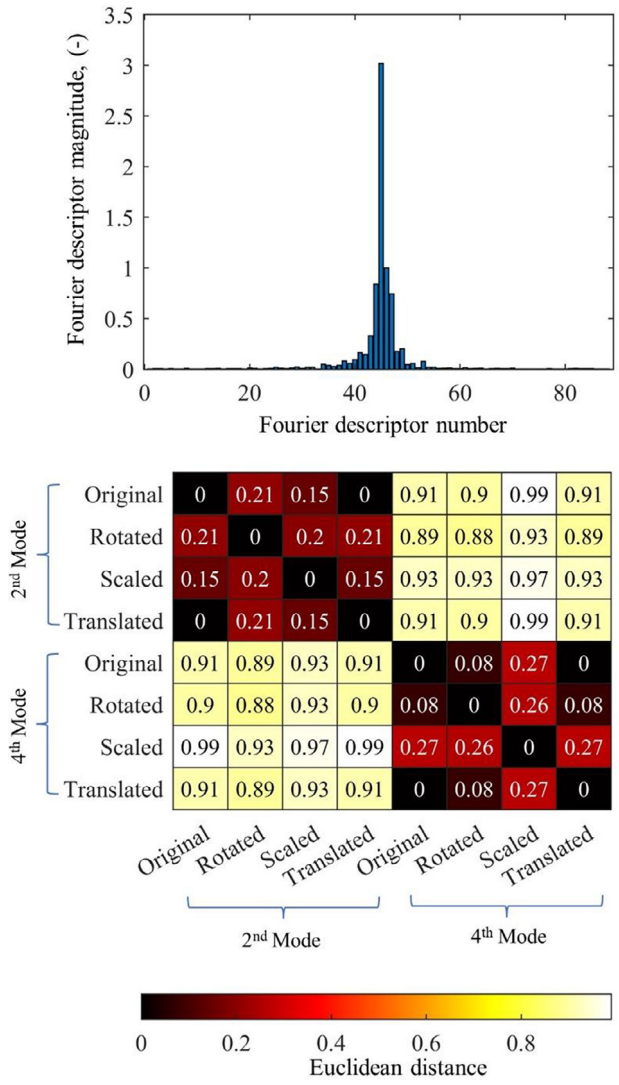

Fig. 11. The 90 Fourier descriptors representing the original contour in Fig. 10 (top). The correlation matrix showing the Euclidean distances between the feature vectors for the four contours at the 4th mode in Fig. 10 and four contours processed using the same ways for the 2nd mode (bottom).

method for selecting the appropriate number of Fourier descriptors is shown in Figs. 8 and 9. A reduction in the number of mismatched facets as the number of Fourier descriptors was increased can be observed, until there were no mismatched facets. Using the percentage of mismatched facets as a criterion for the acceptability of the reconstruction is graphically straightforward and reliable. A heuristic approach was applied to identify the correct mesh density and threshold for the mismatched facets, which were chosen as 2% of the contour size and 10% of the mismatched facets, respectively. As discussed previously, the focus was to compare the general shapes of the nodal region, not the roughness of the contours, therefore the chosen values were appropriate for selecting a minimum number of Fourier descriptors whilst ensuring a reasonable quality reconstruction.

The reasons for using Fourier descriptors are: firstly, data dimensionality was reduced from 10^3 points representing the contour to 10^1 Fourier descriptors; secondly, using the same number of Fourier descriptors made the comparison easier; and thirdly, Fourier descriptors were found to be invariant to simple transformations of the contour. The contours for modes of different specimens are composed of various numbers of points from approximately 1200 to 1900, which makes direct comparison of contours difficult. Therefore, each contour was decomposed

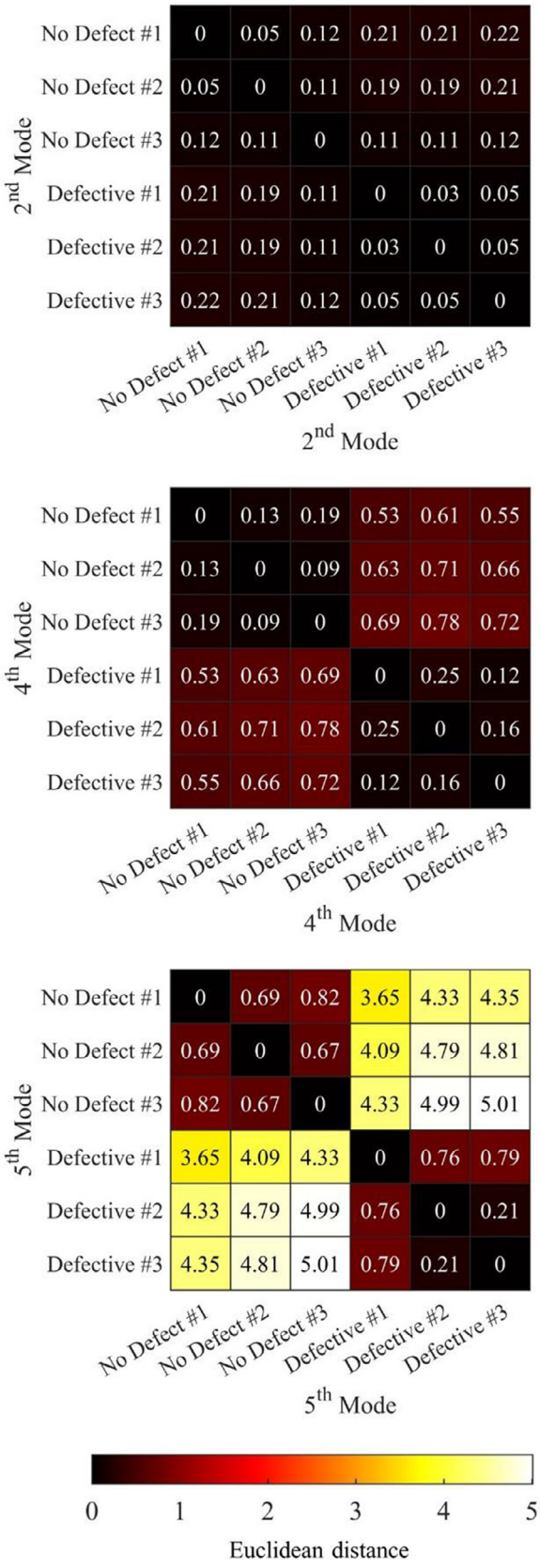

Fig. 12. The correlation matrices showing the pairwise comparisons of the contours for the 2nd mode (top), 4th mode (middle) and 5th mode (bottom) for the whole set of specimens. Each value in the box is the Euclidean distance calculated between the feature vectors.

into 90 Fourier descriptors for easier comparison. Fourier descriptors in this study were made rotation invariant by using the absolute value of the terms, scale invariant by dividing each descriptor by $|F_1|$, and translation invariant by omitting the term $\frac{|F_0|}{|F_1|}$. This invariance was verified by decomposing the four contours at the 4th mode in Fig. 10 and four contours at the 2nd mode. The comparisons made in Fig. 11 show that no matter which one of the three modifications is made to the original contour of the 2nd mode and the 4th mode, the Euclidean distances between the contours of either the 2nd mode or the 4th mode are small, i.e., less than 0.3. These invariance characteristics provide more flexibility when performing the experiment. For example, if the camera position was changed or the attachment point of the stinger on the specimen moved when changing specimens, this would result in slightly different fringe patterns. However, using the technique introduced in this paper, the feature vector of the transformed fringe pattern would not significantly change and thus comparisons could still be made. It could also simplify the comparison of fringe patterns from experiments with simulated mode shapes, by eliminating the need to carefully align the datasets prior to making comparisons. The Euclidean distance between the contours of the 2nd mode and the 4th mode is three to four times larger than that between the contours of either the 2nd mode or the 4th mode, as shown in the correlation matrix in Fig. 11. This indicates that the technique can also be used to distinguish different mode shapes quantitatively.

It has been shown that the existence of in-plane fibre waviness can be identified by comparing the specific mode shapes. The Euclidean distance was used to assess the similarity between two contours representing the nodal regions in mode shapes. The contours for the 1st and the 3rd mode shape of all the specimens appear to be largely horizontal lines that lack significant features which can be used for comparison, therefore no correlation matrices were generated for these two modes. The ratio r_i quantifies the contrast between the defective and defect-free specimens in the correlation matrices in Fig. 12. The value of r_i increases as the vibration mode number increases, from 1.88 to 4.67, and then to 6.14 for the 2nd, 4th, and 5th mode respectively. This indicates that the presence of fibre waviness has no significant effect on the contours for the 2nd mode. However, both the 4th mode and the 5th mode show strong evidence that fibre waviness has a significant effect, and that the 5th mode is the most affected by waviness. The technique offers a high sensitivity that can discern differences between the fringe patterns that are not obvious. This is because by manually observing the fringe patterns for the 4th mode in Fig. 5, the difference between the defect-free and defective specimens is not noticeable. However, the technique still captured this minor difference and generate a distinct correlation matrix shown in Fig. 12. The study represents an advance compared with earlier work [8] because, not only are the differences in mode shapes caused by defects captured by AF-ESPI, but these differences are quantified. The technique is robust for identifying in-plane waviness in carbon fibre reinforced laminates, which could be further utilised as a quality inspection technique in industry for identifying defective components. The technique could also be used to quantify the severity of defects based on how much they change the mode shape of a component.

The timescales for acquiring resonant frequencies, obtaining fringe patterns of mode shapes, and image processing are of the order of seconds once the experimental set-up has been completed. Hammer-based modal analysis was adopted in this study for simplicity; however, the whole process of detection could be made into a fully automated system by changing the excitation method from hammer-based to loudspeaker-based. Thus, the technique could be developed to be contact-free and boost the detection efficiency further. Currently, the most commonly used non-destructive techniques for detecting fibre waviness are ultrasonic C-scan [18], eddy current testing [19] and X-ray computed tomography [20]. Ultrasonic C-scan and eddy current testing require the movement of probes to scan every region of a component to identify the existence of defects, and the frequencies of the probes need to be changed often to achieve the desired penetration depths in order to generate a 3D fibre orientation map. These procedures are time-consuming and thus unsuitable for fast on-site inspections. X-ray computed tomography is not applicable for large components and special care needs to be taken due to radiation risks. Additionally, the three techniques require detailed knowledge and expertise for the analysis of the generated images to interpret whether the detected defects are critical. The technique developed in this study cannot provide a full-scale image of a composite being inspected, but it is more efficient and reveals the overall effect of waviness defects. More importantly, it can quantify the severities of defects. Therefore, it is more suitable for establishing an acceptance or rejection criterion for decision makers.

5. Conclusions

A novel technique using AF-ESPI based modal analysis has been developed for identifying the existence of in-plane fibre waviness in carbon fibre reinforced laminates. Modal analysis was used to obtain the first five resonant frequencies, and the AF-ESPI technique was used to obtain the fringe patterns representing the corresponding mode shapes. The nodal regions were extracted from the fringe patterns using a specially-developed algorithm incorporating DBSCAN. Fourier descriptors were used to reduce data dimensionality and quantify the difference between contours of the nodal regions. A method for selecting an appropriate number of Fourier descriptors to represent a contour by a feature vector was also introduced, which can provide the minimum number such that the nodal region is acceptably represented. The method is based on thresholding the percentage of mismatched facets, which is graphically straightforward and robust. The contours of the nodal regions were compared by calculating the Euclidean distance between pairwise feature vectors, which showed that higher vibration modes can be used for identifying the presence of fibre waviness. This technique could be used for quality assurance of composite components after they have been manufactured.

Declaration of Competing Interest

The authors declare that they have no known competing financial interests or personal relationships that could have appeared to influence the work reported in this paper.

CRediT authorship contribution statement

X.N. Li: Conceptualization, Methodology, Investigation, Software, Writing – original draft. **P.C. Sung:** Methodology, Investigation. **E.A. Patterson:** Supervision, Writing – review & editing. **W.C. Wang:** Supervision, Writing – review & editing. **W.J.R. Christian:** Supervision, Writing – review & editing.

Data Availability

The authors are unable or have chosen not to specify which data has been used.

Acknowledgements

Xiaonan Li was the recipient of a scholarship from the University of Liverpool and National Tsing Hua University dual PhD programme.

References

[1] Kulkarni P, Mali KD, Singh S. An overview of the formation of fibre waviness and its effect on the mechanical performance of fibre reinforced polymer composites. Compos Part A Appl Sci Manuf 2020:137.
[2] Lee SK, Kim MW, Park CJ, Chol MJ, Kim G, Cho JM, et al. Effect of fiber orientation on acoustic and vibration response of a carbon fiber/epoxy composite plate: natural vibration mode and sound radiation. Int J Mech Sci 2016;117:162–73.

[3] Kumar Samal P, Pruthvi IS, Suresh BS. Effect of fiber orientation on vibration response of glass epoxy composite beam. Mater Today Proc 2021;43:1519–25.
[4] Chan WS, Wang JS. Influence of fiber waviness on the structural response of composite laminates. J Thermoplast Compos Mater 1994;7(3):243–60.
[5] Wykes C. Use of electronic speckle pattern interferometry (ESPI) in the measurement of static and dynamic surface displacements. Opt Eng 1982;21(3).
[6] Romero G. Study of a vibrating plate: comparison between experimental (ESPI) and analytical results. Opt Lasers Eng 2003;40(1-2):81–90.
[7] Dai X, Shao X, Geng Z, Yang F, Jiang Y, He X. Vibration measurement based on electronic speckle pattern interferometry and radial basis function. Optics Commun. 2015;355:33–43.
[8] Wang WC, Su CW, Liu PW. Full-field non-destructive analysis of composite plates. Compos.Part A Appl Sci Manuf 2008;39(8):1302–10.
[9] Wang WC, Hsu JS. Investigation of vibration characteristics of bonded structures by time-averaged electronic speckle pattern interferometry. Opt Lasers Eng 2010;48(10):958–65.
[10] Christian WJR, DiazDelaO FA, Atherton K, Patterson EA. An experimental study on the manufacture and characterization of in-plane fibre-waviness defects in composites. R Soc Open Sci 2018;5(5).
[11] Gonzalez R, Woods R. Digital image processing. 4 ed. New York: Pearson; 2018.
[12] Bradley D, Roth G. Adaptive thresholding using the integral image. J Gr Tools 2011;12(2):13–21.
[13] Ester M, Kriegel HP, Sander J, Xu X. A density-based algorithm for discovering clusters in large spatial databases with noise. In: Proceedings of the Second International Conference on Knowledge Discovery in Databases and Data Mining, KDD-96; 1996. p. 226–31.
[14] Schubert E, Sander J, Ester M, Kriegel HP, Xu X. DBSCAN revisited, revisited: why and how you should (Still) use DBSCAN. ACM Trans Datab Syst 2017;42(3):1–21.
[15] Kauppinen H, Seppanen T, Pietikainen M. An experimental comparison of autoregressive and fourier-based descriptors in 2-D shape classification. IEEE Trans Pattern Anal Mach Intell 1995;17:201–7.
[16] Dalitz C, Brandt C, Goebbels S, Kolanus D. Fourier descriptors for broken shapes. EURASIP J Adv Signal Process 2013;2013(1).
[17] Zhang D, Lu G. Review of shape representation and description techniques. Pattern Recognit 2004;37(1):1 -1.
[18] Nelson LJ, Smith RA. Fibre direction and stacking sequence measurement in carbon fibre composites using Radon transforms of ultrasonic data. Compos Part A Appl Sci Manuf 2019;118:1–8.
[19] Mizukami K, Mizutani Y, Todoroki A, Suzuki Y. Detection of in-plane and out-of–plane fiber waviness in unidirectional carbon fiber reinforced composites using eddy current testing. Compos B Eng 2016;86:84–94.
[20] Sutcliffe MPF, Lemanski SL, Scott AE. Measurement of fibre waviness in industrial composite components. Compos Sci Technol 2012;72(16):2016–23.